

## Compact radio sources in M17

Luis F. Rodríguez<sup>1,2</sup>, Ricardo F. González<sup>1</sup>, Gabriela Montes<sup>3</sup>, Hassan M. Asiri<sup>2</sup>, Alejandro C. Raga<sup>4</sup> and Jorge Cantó<sup>5</sup>

l.rodriguez@crya.unam.mx

### ABSTRACT

The classic HII region M17 is one of the best studied across the electromagnetic spectrum. We present sensitive, high angular resolution observations made with the Jansky Very Large Array (JVLA) at 4.96 and 8.46 GHz that reveal the presence of 38 compact radio sources, in addition to the well known hypercompact cometary HII region M17 UC1. For this last source we find that its spectral index of value  $\sim 1$  is due to a gradient in opacity across its face. Of the 38 compact radio sources detected, 19 have stellar counterparts detected in the infrared, optical, or X-rays. Finally, we discuss the nature of the radio emission from the massive binary system CEN 1a and 1b, concluding that both are most probably non-thermal emitters, although the first is strongly time variable and the second is steady.

*Subject headings:* ISM: individual (M17) — stars: individual (CEN 1a, CEN 1b) — radio continuum: stars

### 1. Introduction

The centimeter continuum radiation from classic HII regions is dominated by strong free-free emission from the extended ionized gas present there. However, when observed

---

<sup>1</sup>Centro de Radioastronomía y Astrofísica, Universidad Nacional Autónoma de México, Apdo. Postal 3-72, Morelia, Michoacán 58089, Mexico

<sup>2</sup>Astronomy Department, Faculty of Science, King Abdulaziz University, P.O. Box 80203, Jeddah 21589, Saudi Arabia

<sup>3</sup>Instituto de Astrofísica de Andalucía (IAA), CSIC, Camino Bajo de Huetor 50, 18006 Granada, Spain

<sup>4</sup>Instituto de Ciencias Nucleares, Universidad Nacional Autónoma de México, Apdo. Postal 70-543, CP. 04510, D. F., México

<sup>5</sup>Instituto de Astronomía, Universidad Nacional Autónoma de México, Apdo. Postal 70-264, CP. 04510, D. F., México

with the high angular resolution provided by an interferometer, the extended emission is filtered out and one starts to detect compact sub-arcsecond sources of various natures (see Garay et al. 1987; Churchwell et al. 1987; Felli et al. 1993; Zapata et al. 2004 for the case of Orion A). The brightest of these sources are the hypercompact (HC) HII regions, that trace the ionized gas produced by young OB stars still embedded in dense molecular gas (e.g. Kurtz 2005; Lizano 2008). The externally ionized globules are also sources of free-free radiation and result from the interaction of the UV photons of the OB stars in the region with remaining blobs of neutral gas existing inside the HII region (e.g. Garay et al. 1987). The proplyds (O’Dell et al. 1993) are similar to the externally ionized globules, but in this case the object being ionized is a protoplanetary disk surrounding a young star. The last two known types of free-free emitters are the jets emanating from accreting protostars (Anglada 1996; Eisloffel et al. 2000) and the spherical ionized winds produced by massive stars (e.g. Bieging et al. 1989; Contreras et al. 1996). There are also two types of sources with non-thermal radio continuum emission. Young low-mass stars can have strong magnetospheric activity and emit detectable gyrosynchrotron radiation (André et al. 1988). Finally, there is also strong evidence that systems of massive binary stars can produce synchrotron radiation in the region where their winds collide (e.g. Pittard et al. 2006; Ortiz-León et al. 2011). In Table 1 we present a summary of the characteristics of these different types of compact radio sources.

In this paper we present a sensitive, high angular resolution study made with the Jansky Very Large Array (JVLA) of the National Radio Astronomy Observatory (NRAO)<sup>1</sup> toward the classic HII region M17 (the Omega Nebula, NGC 6618, W38, S45). In § 2 we present the observations, while in § 3 we list and briefly discuss the compact radio sources detected. In § 4 we use our data to present an explanation for the spectral index of order 1 observed in the hypercompact HII region M17 UC1. In § 5 we discuss the time variable sources in our sample, while in § 6 we concentrate on CEN 1a and 1b, the members of the massive binary system that ionizes most of M17. In § 7 we try to model the time-variable emission of CEN 1a in terms of a thermal model, concluding that this is not feasible. Finally, § 8 presents a brief discussion on some of the other individual sources and in § 9 we summarize our conclusions.

---

<sup>1</sup>The NRAO is operated by Associated Universities Inc. under cooperative agreement with the National Science Foundation.

## 2. Observations

The JVLA observations were made at 4.96, 8.46 and 22.46 GHz using two intermediate frequency (IF) bandwidths of 128 MHz each, separated by 128 MHz, and containing both circular polarizations. Each IF was split into 64 channels of 2 MHz each. For the continuum images we averaged the central 54 channels, rejecting five channels at each end of the bandwidth. We observed in three epochs during the year 2011: June 16 (2011.46) and 27 (2011.49), and July 28 (2011.57). This cadence was adopted with the purpose of searching for variability at 4.96 and 8.46 GHz in the timescales of about 10, 30, and 40 days. The observations at 22.46 GHz were made only in the second epoch (2011 June 27) with the purpose of determining better spectral indices. In addition to these timescales, we searched for rapid variability (i.e. in timescales of minutes) during the two hours of each individual run. At all 3 epochs, the JVLA was in the highest angular resolution A configuration.

The data reduction was made using the software package AIPS of NRAO, following the recommendations for JVLA data given in Appendix E of its Cookbook (that can be found in <http://www.aips.nrao.edu/cook.html>). The amplitude calibrator was J1331+3030, with adopted flux densities of 7.392, 5.205 and 2.519 Jy at 4.96, 8.46 and 22.46 GHz, respectively. The phase calibrator was J1832-1035, with the bootstrapped flux densities given in Table 2.

The data were self-calibrated in amplitude and phase and we made images using only visibilities with baselines larger than  $50 \text{ k}\lambda$ , suppressing structures larger than  $\sim 4''$ . The search for variability within each individual run was made without self-calibration, since this procedure tends to smooth out amplitude variations within the time interval where it is applied. At 4.96 and 8.46 GHz we analyzed regions of  $8' \times 8'$  in solid angle, while at 22.46 GHz the region analyzed was  $2' \times 2'$ . At 22.46 GHz our  $4\text{-}\sigma$  sensitivity at the center of the field was  $\sim 0.4 \text{ mJy beam}^{-1}$  and the only source detected was M17 UC1, a well-known hypercompact HII region embedded in the molecular cloud adjacent to the SW of the M17 HII region (Felli et al. 1980). At 4.96 and/or 8.46 GHz we detected a total of 38 compact sources, in addition to M17 UC1. These sources are listed in Table 3. The rms noise of the images is not constant across all the solid angle analyzed for two reasons. First, the primary beam response decreases as we move away from the center of the field (e.g. Cotton & Perley 2010). The correction for this effect increases both signal and noise. In addition, in this region there is an arc-shaped ionization front to the east and northeast of M17 UC1 that makes it noisier than expected (Felli et al. 1984; Johnson et al. 1998). This structure most probably traces the interaction of the ionizing photons of NGC 6618, the cluster ionizing M17, with the molecular clump where M17 UC1 is embedded.

Assuming a typical noise of  $0.05 \text{ mJy beam}^{-1}$  at the center of the field for the 8.46 GHz observations and following Anglada et al. (1998), we expect to detect only about one

background source above  $4\text{-}\sigma$  over all the solid angle analyzed. We can then conclude that practically all the detected sources are related to M17.

### 3. Compact radio sources

In Table 3 we list the 38 detected compact radio sources, giving their positions, flux densities at 8.46 and 4.96 GHz, the resulting spectral index, and their angular size. Most of the sources are unresolved ( $\leq 0''.2$ ). In Table 4 we list the 19 compact radio sources with reported counterparts at other wavelengths (in all cases, stars detected previously at optical, near-infrared, or X-rays). A counterpart was considered to be associated with the JVLA source if its position coincided within  $\leq 1''$  of the radio position. We tried to find systematic differences between the radio sources with and without counterparts by plotting them in a spectral index versus flux density diagram (see Fig. 1). This diagram does not segregate the two classes of source and we tentatively suggest that the radio sources without counterparts are similar to those that have a counterpart, but are very heavily obscured which makes detection difficult at wavelengths other than radio.

### 4. The origin of the spectral index of the hypercompact HII region M17 UC1

This bright source has an angular size of  $\sim 0''.4$ , that at a distance of 1.98 kpc (Xu et al. 2011) implies a diameter of  $\sim 0.004$  pc, falling in the category of the hypercompact HII regions (Kurtz 2005). Its morphology is cometary. For this source we obtain total flux densities of 44, 107, and 194 mJy at 4.96, 8.46, and 22.46 GHz, respectively. These flux densities indicate a spectral index of  $\beta = 0.8 \pm 0.2$  ( $S_\nu \propto \nu^\beta$ ), consistent with the value of  $\beta \simeq 1$  typically found in hypercompact HII regions (Hofner et al. 1996; Kurtz 2002; Sewilo et al. 2004). The reason for this intermediate spectral index remains unknown. Homogeneous HII regions are expected to show  $\beta \simeq 2$  when optically thick (low frequencies) and  $\beta \simeq -0.1$  when optically thin (high frequencies). In these sources the transition from optically-thick to optically-thin occurs in a small frequency range. The indices of  $\beta \simeq 1$  observed in hypercompact HII regions cannot be explained as the result of observing this transition region since they extend over at least an order of magnitude in frequency. An alternative explanation is given by the hierarchical clumping model of Ignace & Churchwell (2004), where it is proposed that the radio continuum energy spectrum comes from an ensemble of spherical clumps. In this model, for example, the spectral index of  $\sim 1$  should be detected all across the face of the nebula.

Taking advantage of the excellent quality of our 8.46 GHz data, we derived the spectral index for M17 UC1 as a function of position. Our 4.96 GHz data does not have enough angular resolution to clearly resolve the source and our 22.46 GHz data is centered on the NGC 6618 cluster and M17 UC1 is located too far from the phase center and the integration is relatively short (a total of 20 minutes on-source). We then used for the comparison with our 8.46 GHz JVLA data, archive VLA data taken at 22.49 GHz in 1982 March 20 under project FELL. For these archive VLA observations the amplitude calibrator was 1331+305, with an adopted flux density of 2.52 Jy and the phase calibrator was 1730–130, with a bootstrapped flux density of  $4.86 \pm 0.01$  Jy. To obtain a reliable astrometry, the position of 1730–130 was updated to the most recently improved value provided by the JVLA Calibrator Manual. Both the 8.46 and 22.46 GHz observations were made in the A configuration. To obtain comparable (u,v) coverage at both frequencies we did not include the two inner antennas at each arm for the 8.46 GHz observations and the three outer antennas at each arm for the 22.46 GHz observations. The resulting (u,v) coverages are shown in Figure 2. The images at both frequencies were restored using the synthesized beam of the 8.46 GHz observations.

In Figure 3 we show the contour images at 8.46 and 22.49 GHz as well as the derived spectral index from these two images. The spectral index image shows that there is a smooth gradient from values of  $\sim 2$  (optically-thick emission) near the head of the cometary nebula to values of  $\sim -0.1$  (optically-thin emission) near the tail. This result suggests that, at least in this hypercompact HII region the intermediate value of  $\sim 1$  for the spectral index comes from a gradient in optical depth across the face of the nebula. We speculate that if this is the explanation for the spectral index found in other hypercompact HII regions, they should show a cometary morphology when observed with sufficiently high angular resolution. For this effect to be observable at frequencies similar to those used here, we need objects with large average emission measures, of order  $\sim 10^9 \text{ cm}^{-6} \text{ pc}$ , so that they can present significant optical depths at frequencies of order 15 GHz.

## 5. Time-variable radio sources

Of the 38 compact sources detected, two of them show large variations between the three observing runs. The first time variable source is CEN 1a, whose flux densities are listed in Table 5. Images at the three epochs are shown in Fig. 4. This source was not detected in the first two epochs but in the last epoch it became quite bright, with a flux density about an order of magnitude larger than the  $4\text{-}\sigma$  upper limits obtained for the first two epochs. The other variable source was the B1 star NGC 6618 B 159, whose flux densities are given in Table 6.

In addition to possible long term variability between runs, we also searched for short timescale variability within the individual runs. Our procedure to search for such variability was the following. First, images of the source of interest were made with the AIPS task IMAGR for each observation epoch. With the AIPS task JMFIT, the precise position of the primary component was determined. The  $(u, v)$  data were recentered at the position of the main component using the AIPS task UVFIX. With these new  $(u, v)$  data, the real and imaginary parts of the interferometer data were plotted as a function of time, averaged over the  $(u, v)$  plane. The real part gives us information on the flux density of the source and the imaginary part on its position and symmetry. We then averaged over time in bins of approximately 10 minutes. A detailed description of this technique is given by Neria et al. (2010). The flux density as a function of time for the two time variable sources during a given run is shown in Figures 5 (CEN 1a) and 6 (NGC 6618 B 159). No fast variability (hours or less) was detected for these sources.

Finally, of the seven sources detected by Rodríguez et al. (2009), only one is not detected by us. This source is named VLA 2 by Rodríguez et al. (2009) and is located at the position  $\alpha(2000) = 18^h 20^m 29^s.84$ ;  $\delta(2000) = 16^\circ 10' 15''.2$ . Rodríguez et al. (2009) reported an 8.46 GHz flux density of  $1.3 \pm 0.1$  mJy, while from the images made from the concatenated  $(u, v)$  data we set a  $4\text{-}\sigma$  upper limit of 0.07 mJy. As noted before, also CEN 1a is time-variable. The remaining five sources detected by Rodríguez et al. (2009) were detected by us at similar flux densities.

## 6. CEN 1a and CEN 1b

CEN 1a and CEN 1b are a massive binary system (with angular separation of  $\sim 1''.8$ ; Chini et al. 1980). The O4 V stars that form this binary system are the main ionizing sources of the M17 H II region (e. g. Hoffmeister et al. 2008) and the brightest X-ray objects in the zone (Broos et al. 2007). CEN 1a and CEN 1b were first detected as radio sources by Rodríguez et al. (2009). Our data provides new information on these radio sources. While CEN 1a is strongly time-variable (see Table 4), CEN 1b appears to be a steady source. The flux densities found by us for 2011 June-July are consistent with the flux densities reported by Rodríguez et al. (2009) for 1988 October and 2000 December. The available information suggests that CEN 1b is constant over timescales of decades. Its spectral index, as derived from the 2011 June-July observations is  $-0.7 \pm 0.2$ , suggesting optically-thin synchrotron emission.

In contrast, CEN 1a is strongly variable. As noted above, it was detected only in the last epoch of our observations, showing a spectral index of  $-0.1 \pm 0.1$ . As was pointed out by

Rodríguez et al. (2009), the flux density expected from a stellar wind in a single star scenario is too low ( $\sim 0.1$  mJy at 8.46 GHz) to account for the relatively large flux density detected ( $\sim 2.6$  mJy at 8.46 GHz). This fact and the strong variability observed suggest a binary origin for the source, with the emission arising from a wind-wind colliding region (WCR) between the stars forming the binary system. In this binary scenario, the variability is thought to be the result of an eccentric orbit and/or a high inclination angle of the orbital plane. In this context, the spectral index observed could be compatible with both optically-thin thermal emission (Pittard 2010) and non-thermal (synchrotron) emission (Contreras et al. 1997), arising both from the WCR. Its flat value is in agreement with synchrotron emission being affected by free-free absorption from the unshocked winds, turning the negative value expected from intrinsic optically-thin synchrotron emission into the flat spectrum observed for CEN 1a. The thermal contribution from a WCR is expected to increase the flux density only a factor of a few with respect to that from the single stellar wind (Stevens 1995, Pittard 2010). On the other hand, the non-thermal emission has been observed to increase the flux by more than one order of magnitude with respect to the minimum states of the radio light curves of colliding wind binaries (CWB; e.g. HD 168112; Blomme et al. 2005). Thus, the strong increase in the flux observed in CEN 1a suggests a non-thermal origin for the emission detected.

However, given that the spectral index is consistent with optically-thin free-free emission, we have considered thermal emission models, but cannot find any that are reasonable and match the observations. We conclude that the observed radio emission from CEN 1a most probably has a non-thermal nature and that the observed flat spectrum is consistent with a combination of synchrotron emission and free-free absorption, as noted before. Non-thermal emission in massive stars is usually attributed to them being binary systems, with the emission coming from the wind collision region. Alternatively, the radio emission could be coming from Fermi acceleration in wind shocks of a single star due to the radiation-driven instability (Lucy & White 1980; White & Chen 1994). This system provides the opportunity to study simultaneously two stars, a variable one (CEN 1a) and a steady one (CEN 1b) and to try to understand what is the reason for their different behaviours.

## 7. Notes on individual sources

### 7.1. JVLA 3

This radio source is within a few arcsec of the bright infrared object KW (Kleinmann & Wright 1973; Povich et al. 2009) and it is probably associated with it.

## 7.2. JVLA 35

This source is remarkable because it is clearly detected at 8.46 GHz, but not at 4.96 GHz (see Figure 7), resulting in a spectral index of  $\geq 2.9 \pm 0.6$ . This spectral index is consistent with optically-thick free-free emission, optically-thick synchrotron or even with optically thin dust emission. The source is arc-shaped (see Figure 7) and could be tracing the edge of a heated dust globule. There are no known counterparts to this source in the SIMBAD database. We also searched unsuccessfully for a counterpart in the GLIMPSE catalog of candidate young stellar objects with a high probability of association with the M17 complex (Povich et al. 2009). Its unusual radio spectrum deserves further study.

## 8. Conclusions

We presented sensitive, high angular resolution observations made with the Jansky Very Large Array (JVLA) at 4.96 and 8.46 GHz toward the HII region M17. Our main conclusions are listed in what follows.

1. We detected 38 compact radio sources, practically all associated with the region. Only 19 of these sources have counterparts, in all cases stars previously detected at infrared, optical, or X-rays. We argue that the radio sources without counterparts are similar to those with counterparts, but that they are heavily obscured, which makes detection difficult at wavelengths other than radio.

2. We studied the spectral index of the hypercompact HII region M17 UC1, finding that its spectral index of value  $\sim 1$  is due to a gradient in optical depth across its face. We speculate that this type of gradient could explain similar spectral indices detected in other hypercompact HII regions. In this case, all these sources should show a cometary morphology.

3. We discussed the nature of the radio emission from the massive binary system CEN 1a and 1b, concluding that both are most probably non-thermal emitters, although the first one is highly time variable and the second one is steady. Non-thermal emission in massive stars is usually attributed to them being binary systems, with the emission coming from the wind collision region. This system provides the opportunity to study simultaneously two stars, a variable one (CEN 1a) and a steady one (CEN 1b) and to try to understand the reasons for their different behaviours.

J.C., R.F.G., A.C.R., and L.F.R. acknowledge the financial support of DGAPA, UNAM



and CONACyT, México. The National Radio Astronomy Observatory is a facility of the National Science Foundation operated under cooperative agreement by Associated Universities, Inc.

## REFERENCES

- Andre, P., Montmerle, T., Feigelson, E. D., Stine, P. C., & Klein, K.-L. 1988, *ApJ*, 335, 940
- Anglada, G. 1996, *Radio Emission from the Stars and the Sun*, 93, 3
- Anglada, G., Villuendas, E., Estalella, R., et al. 1998, *AJ*, 116, 2953
- Bieging, J. H., Abbott, D. C., & Churchwell, E. B. 1989, *ApJ*, 340, 518
- Blomme, R., van Loo, S., De Becker, M., et al. 2005, *A&A*, 436, 1033
- Broos, P. S., Feigelson, E. D., Townsley, L. K., Getman, K. V., Wang, J., Garmire, G. P., Jiang, Z., & Tsuboi, Y. 2007, *ApJS*, 169, 353
- Bumgardner, T. E. 1992, M.S. thesis, Ohio State Univ., Columbus
- Cantó, J., Raga, A. & D'Alessio, P. 2000, *MNRAS*, 313, 656
- Chini, R., Elsaesser, H., & Neckel, T. 1980, *A&A*, 91, 186
- Churchwell, E., Felli, M., Wood, D. O. S., & Massi, M. 1987, *ApJ*, 321, 516
- Contreras, M. E., Rodriguez, L. F., Gomez, Y., & Velazquez, A. 1996, *ApJ*, 469, 329
- Contreras, M. E., Rodriguez, L. F., Tapia, M., et al. 1997, *ApJ*, 488, L153
- Cotton, W. D. & Perley, R. 2010, *OBIT Development Memo Series No. 17*
- Eisloffel, J., Mundt, R., Ray, T. P., & Rodriguez, L. F. 2000, *Protostars and Planets IV*, 815
- Felli, M., Johnston, K. J., & Churchwell, E. 1980, *ApJ*, 242, L157
- Felli, M., Churchwell, E., & Massi, M. 1984, *A&A*, 136, 53
- Felli, M., Taylor, G. B., Catarzi, M., Churchwell, E., & Kurtz, S. 1993, *A&AS*, 101, 127
- Garay, G., Moran, J. M., & Reid, M. J. 1987, *ApJ*, 314, 535
- Hoffmeister, V. H., Chini, R., Scheyda, C. M., Schulze, D., Watermann, R., Nürnberger, D., & Vogt, N. 2008, *ApJ*, 686, 310

- Hofner, P., Kurtz, S., Churchwell, E., Walmsley, C. M., & Cesaroni, R. 1996, *ApJ*, 460, 359
- Ignace, R., & Churchwell, E. 2004, *ApJ*, 610, 351
- Johnson, C. O., Depree, C. G., & Goss, W. M. 1998, *ApJ*, 500, 302
- Kleinmann, D. E., & Wright, E. L. 1973, *ApJ*, 185, L131
- Kurtz, S. 2002, *Hot Star Workshop III: The Earliest Phases of Massive Star Birth*, 267, 81
- Kurtz, S. 2005, *Massive Star Birth: A Crossroads of Astrophysics*, 227, 111
- Lizano, S. 2008, *Massive Star Formation: Observations Confront Theory*, 387, 232
- Lucy, L. B., & White, R. L. 1980, *ApJ*, 241, 300
- O’Dell, C. R., Wen, Z., & Hu, X. 1993, *ApJ*, 410, 696
- Ortiz-León, G. N., Loinard, L., Rodríguez, L. F., Mioduszewski, A. J., & Dzib, S. A. 2011, *ApJ*, 737, 30
- Pittard, J. M., Dougherty, S. M., Coker, R. F., O’Connor, E., & Bolingbroke, N. J. 2006, *A&A*, 446, 1001
- Pittard, J. M. 2010, *MNRAS*, 403, 1633
- Povich, M. S., Churchwell, E., Bieging, J. H., et al. 2009, *ApJ*, 696, 1278
- Raga, A.C., Cantó, J., Binette, L. & Calvet N. 1990, *ApJ*, 364, 601
- Rodríguez, L. F., González, R. F., & Montes, G. 2009, *Rev. Mexicana Astron. Astrofis.*, 45, 273
- Sewilo, M., Churchwell, E., Kurtz, S., Goss, W. M., & Hofner, P. 2004, *ApJ*, 605, 285
- Stevens, I. R. 1995, *MNRAS*, 277, 163
- White, R. L., & Chen, W. 1994, *Ap&SS*, 221, 295
- Xu, Y., Moscadelli, L., Reid, M. J., et al. 2011, *ApJ*, 733, 25
- Zapata, L. A., Rodríguez, L. F., Kurtz, S. E., & O’Dell, C. R. 2004, *AJ*, 127, 2252

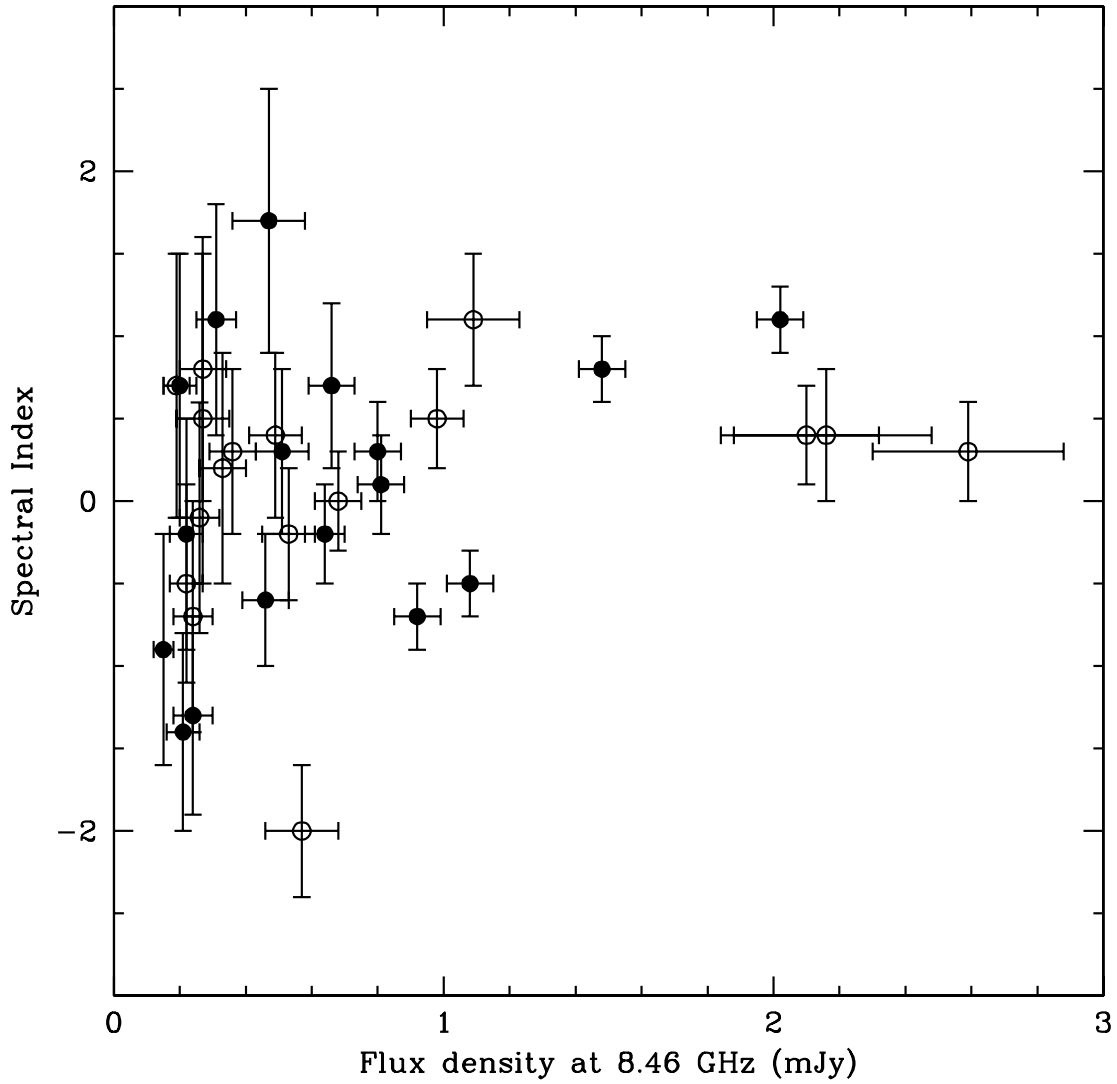


Fig. 1.— Spectral index versus flux density at 8.46 GHz for the 32 compact radio sources with determined spectral index. The empty circles indicate the sources without counterparts, while the solid circles indicate the sources with counterparts.

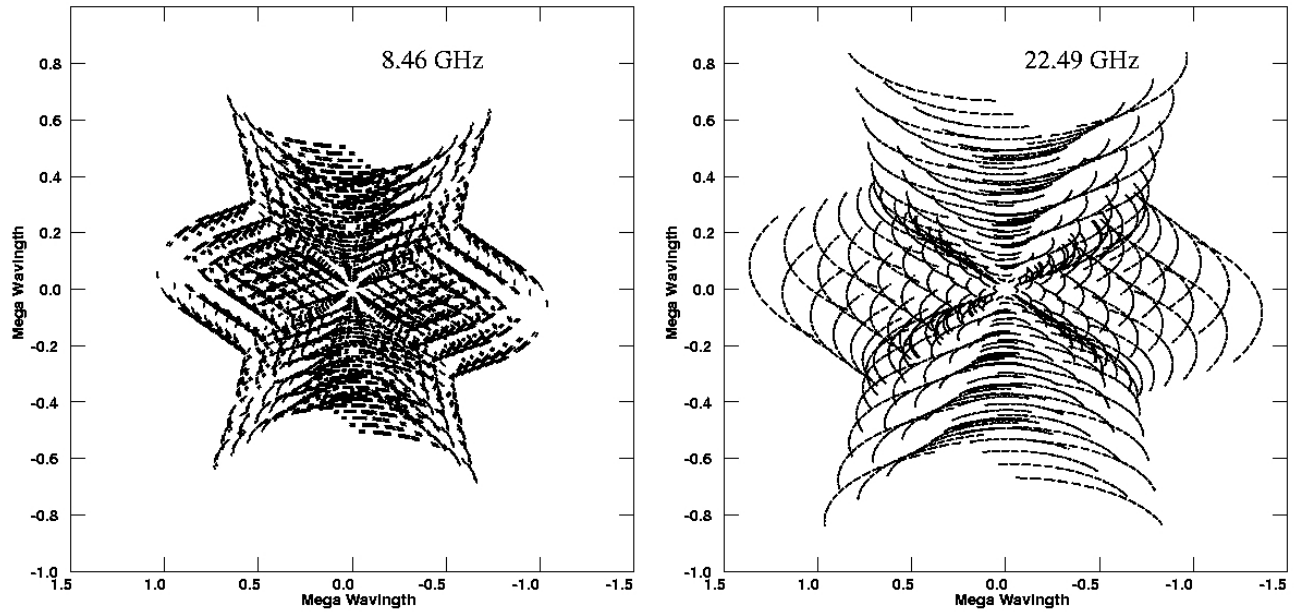


Fig. 2.— (u,v) coverage of the 8.46 (left) and 22.49 GHz (right) observations used to estimate the spectral index of M17 UC1.

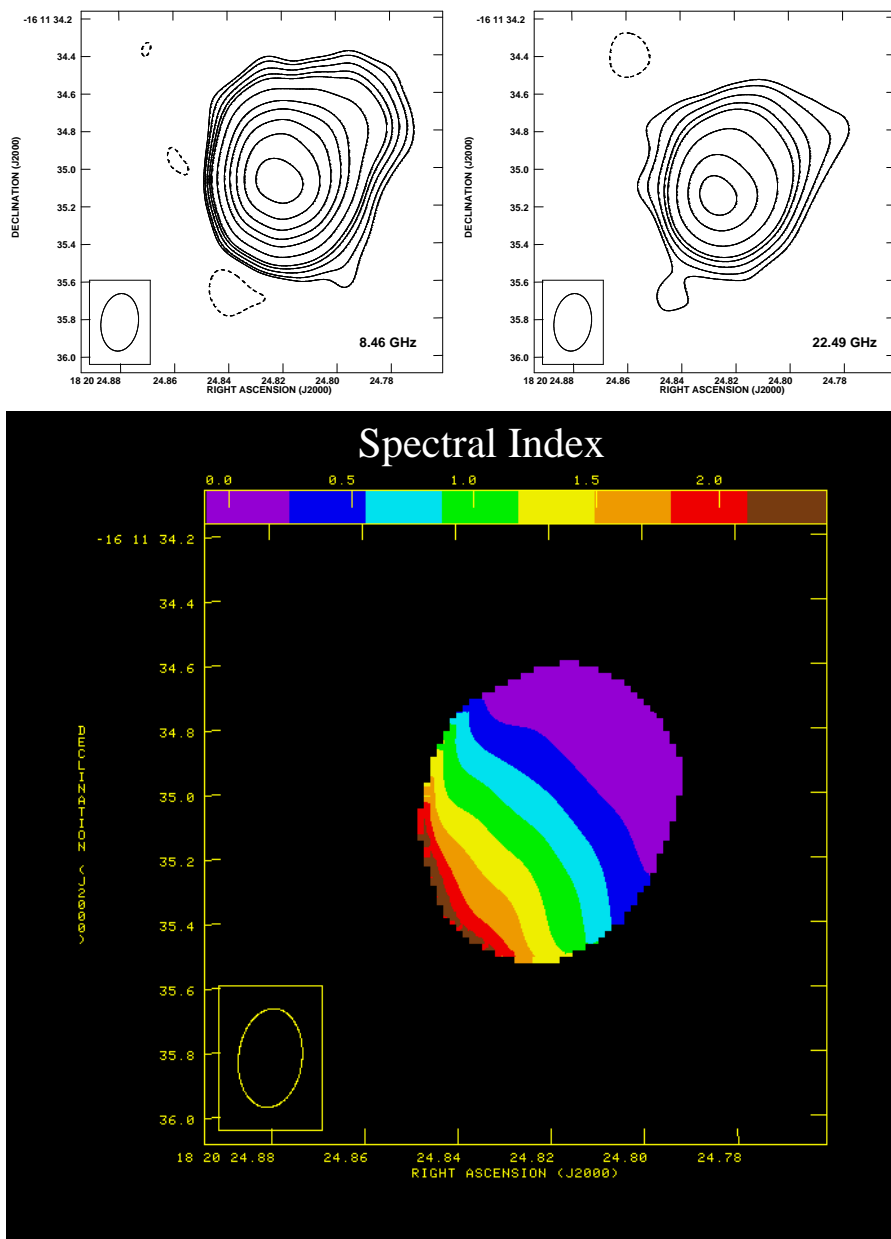


Fig. 3.— (Top left) JVLVA contour image of M17 UC1 at 8.46 GHz. (Top right) VLA contour image of M17 UC1 at 22.49 GHz. For these two images the contours are -4, 4, 6, 10, 15, 20, 40, 80, 120, 180, 260, and 360 times  $0.065 \text{ mJy beam}^{-1}$  (8.46 GHz) and  $0.45 \text{ mJy beam}^{-1}$  (22.49 GHz), the respective rms noise of each image. (Bottom) Color image of the spectral index as a function of position, as derived from the 8.46 and 22.49 GHz images. The color bar on top of this image gives the coding for the spectral index. The half power contour of the beam is  $0''.31 \times 0''.20$  with  $PA = -7^\circ$  and it is shown in the bottom left corner of the images.

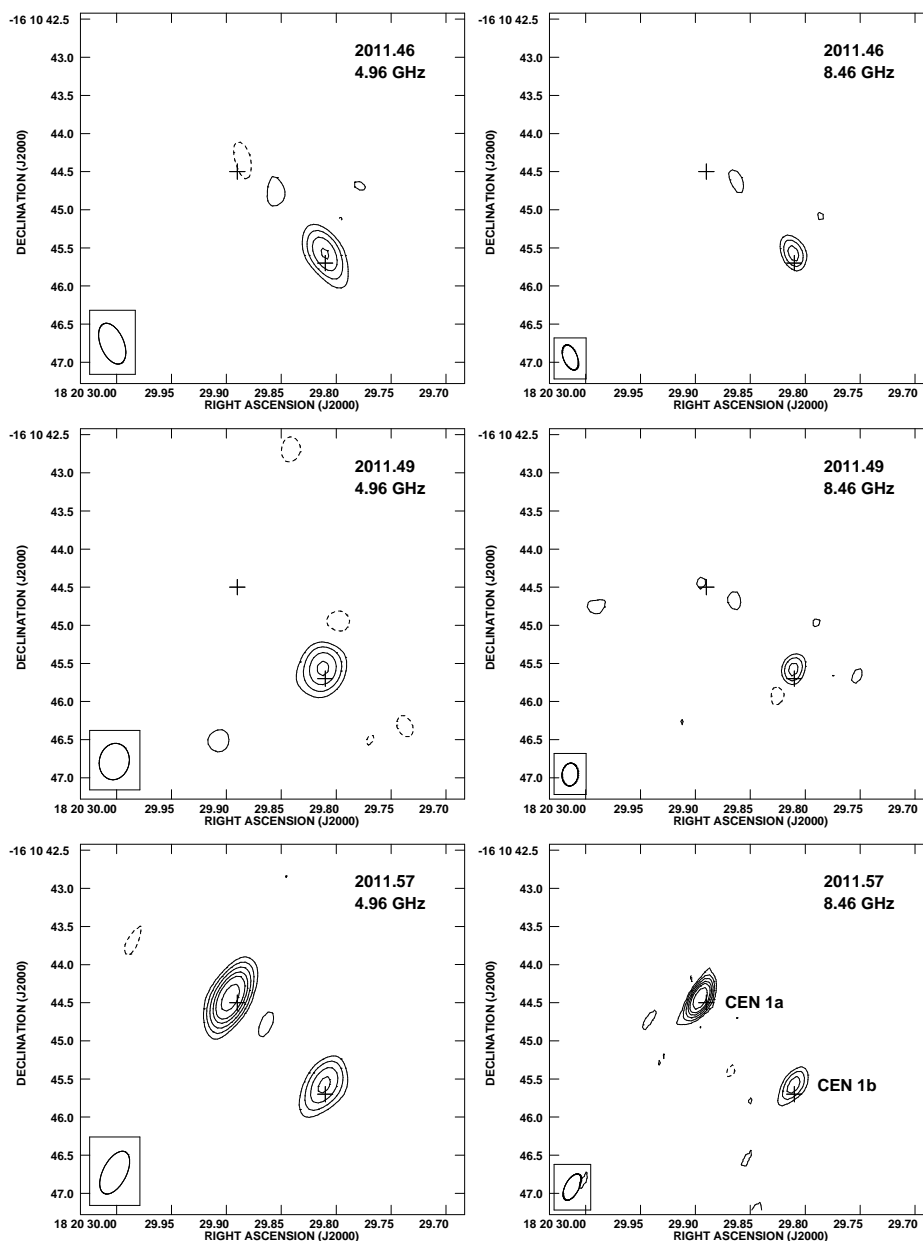


Fig. 4.— JVLA images of the CEN 1 region. In each panel the crosses mark the X-ray positions of CEN 1a and CEN 1b given by Broos et al. (2007). (Left column) Images at 4.96 GHz for the three epochs of observation. Contours are  $-3, 3, 6, 10, 15, 20$  and  $30$  times  $72 \mu\text{Jy beam}^{-1}$ , the average rms noise of the images. The half power contour of the synthesized beams is shown in the bottom left corner of each panel. (Right column) Same as in the left column, but for the frequency of  $8.46$  GHz. Contours are given times  $57 \mu\text{Jy beam}^{-1}$ , the average rms noise of the images.

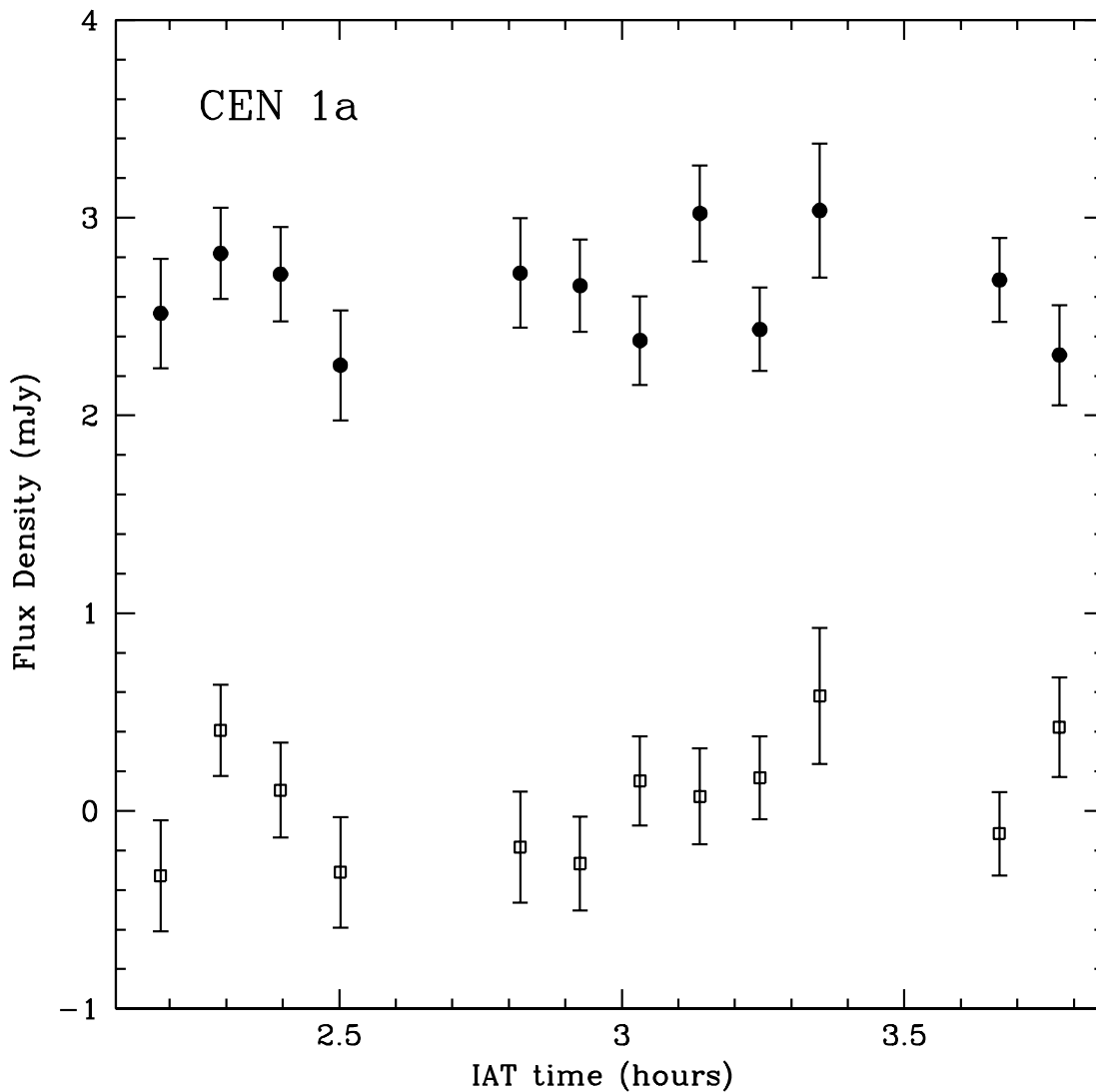


Fig. 5.— Real (filled circles) and imaginary (empty squares) components of the interferometer data for CEN 1a at 8.46 GHz for 2011 July 28 as a function of international atomic time (IAT). The real component is consistent with no significant variability over the period of the observation and a constant flux density of  $2.6 \pm 0.1$  mJy. The imaginary component is consistent with zero, indicating that the source is symmetric about the phase center (the origin of the visibility plane) and has no significant structure on these spatial scales.

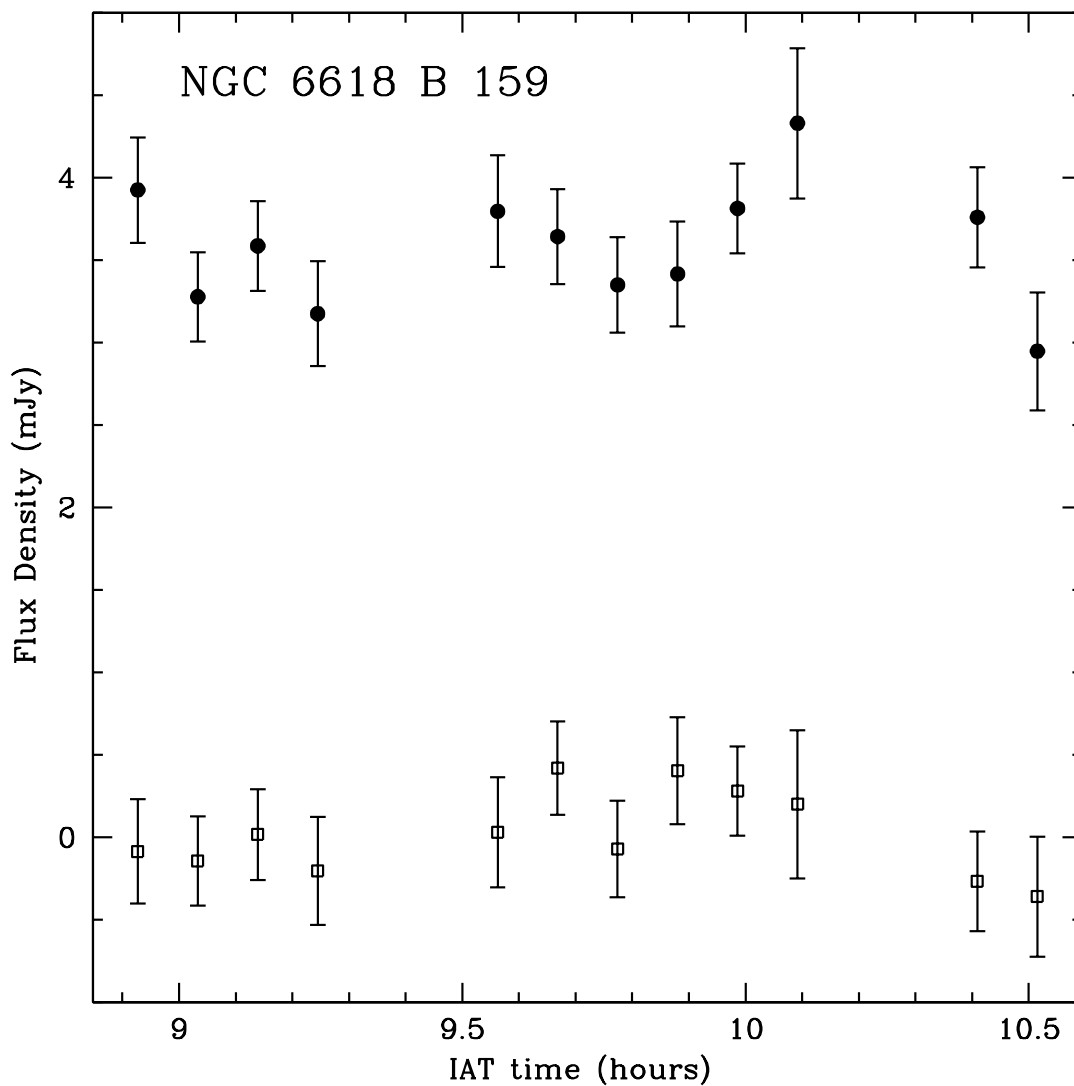


Fig. 6.— Real (filled circles) and imaginary (empty squares) components of the interferometer data for NGC 6618 B 159 at 8.46 GHz for 2011 June 16 as a function of international atomic time (IAT). The real component is consistent with no significant variability over the period of the observation and a constant flux density of  $3.8 \pm 0.1$  mJy. The imaginary component is consistent with zero, indicating that the source is symmetric about the phase center (the origin of the visibility plane) and has no significant structure on these spatial scales.



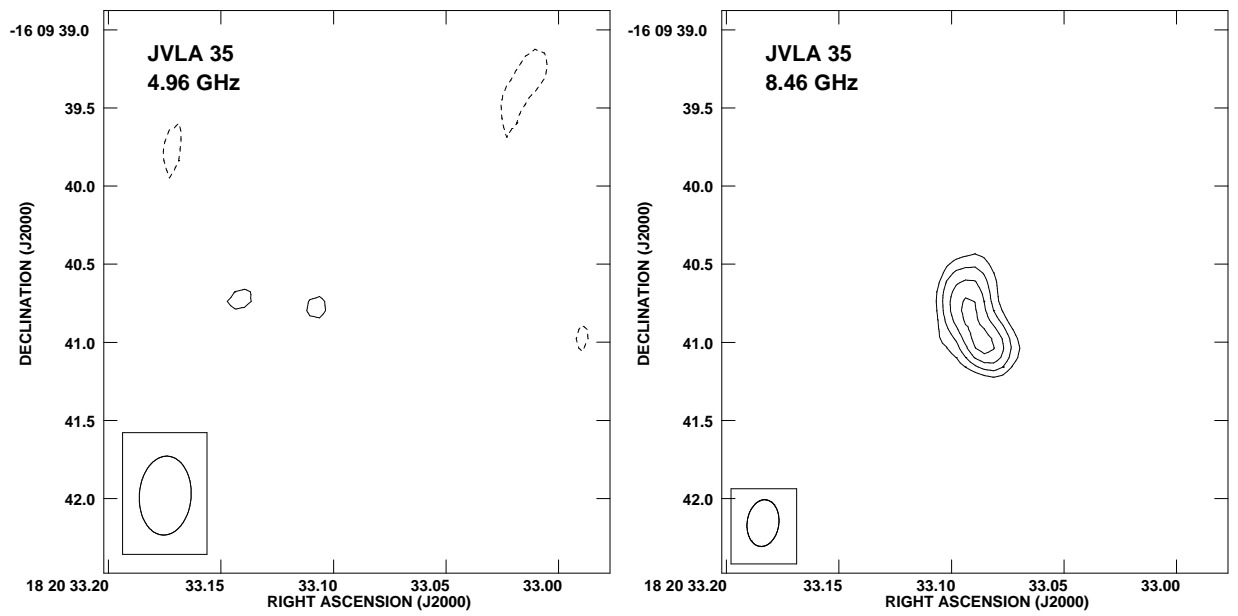


Fig. 7.— J2000 images of the source J2000 182033.20-160939.0 at 4.96 (left) and 8.46 GHz (right). Contours are  $-3, 3, 4, 5,$  and  $6$  times  $30\mu\text{Jy beam}^{-1}$ . The source is clearly detected at 8.46 GHz, but not at 4.96 GHz. The half power contour of the synthesized beam is shown in the bottom left corner of the images and is  $0''.51 \times 0''.33$  with  $PA = -4^\circ$  for the 4.96 GHz image and  $0''.30 \times 0''.20$  with  $PA = -8^\circ$  for the 8.46 GHz image.

Table 1: Characteristics of compact radio continuum sources in HII regions.

Class of Source	Emission Mechanism	Spectral Index	Polarization	Time Variability	Morphology	Excitation
HC HII region	Free-free	$\sim 1$	No	No	Various	Internal
Ionized globule	Free-free	$\sim -0.1$	No	No	Cometary	External
Proplyds	Free-free	$\sim -0.1$	No	No	Cometary	External
Jet	Free-free	$\sim 0.6$	No	Yes	Elongated	Internal
Spherical wind	Free-free	$\sim 0.6$	No	No	Unresolved	Internal
Low-mass protostars	Gyrosynchrotron	$-2 - +2$	Circular	Yes	Unresolved	Internal
Massive binary stars	Synchrotron	$\sim -0.7$	Linear	Yes	Cometary	Internal

Table 2: Bootstrapped flux densities for the phase calibrator J1832-1035.

Frequency (GHz)	2011 Jun 16 (Jy)	2011 Jun 27 (Jy)	2011 Jul 28 (Jy)
4.96	$1.359 \pm 0.003$	$1.315 \pm 0.002$	$1.314 \pm 0.002$
8.46	$1.433 \pm 0.004$	$1.404 \pm 0.002$	$1.404 \pm 0.003$
22.46	—	$1.072 \pm 0.006$	—

Table 3. Compact radio continuum sources in M17

JVLA Number	Position <sup>a</sup>		Flux Density(mJy)		Spectral Index	Angular Size <sup>b</sup>
	$\alpha(2000)$	$\delta(2000)$	8.46 GHz	4.96 GHz		
1	18 20 13.335	-16 12 50.69	$\leq 0.48 \pm 0.12$	$1.14 \pm 0.10$	$\leq -1.6 \pm 0.5$	U
2	18 20 17.575	-16 12 21.52	$0.57 \pm 0.11$	$1.63 \pm 0.13$	$-2.0 \pm 0.4$	0".4
3	18 20 19.475	-16 13 29.87	$0.33 \pm 0.06$	$\leq 0.20 \pm 0.05$	$\geq +0.9 \pm 0.6$	U
4	18 20 21.435	-16 12 06.81	$0.21 \pm 0.05$	$0.45 \pm 0.11$	$-1.4 \pm 0.6$	U
5	18 20 21.637	-16 11 17.91	$0.66 \pm 0.07$	$0.46 \pm 0.10$	$+0.7 \pm 0.5$	U
6	18 20 22.369	-16 12 04.95	$0.27 \pm 0.08$	$0.21 \pm 0.09$	$+0.5 \pm 1.0$	U
7	18 20 25.317	-16 11 48.74	$1.09 \pm 0.14$	$0.60 \pm 0.11$	$+1.1 \pm 0.4$	0".3
8	18 20 25.496	-16 10 53.77	$0.47 \pm 0.11$	$0.19 \pm 0.07$	$+1.7 \pm 0.8$	U
9	18 20 25.297	-16 11 39.83	$2.16 \pm 0.32$	$1.70 \pm 0.31$	$+0.4 \pm 0.4$	0".6
10	18 20 26.239	-16 11 15.85	$0.68 \pm 0.07$	$0.69 \pm 0.09$	$+0.0 \pm 0.3$	U
11	18 20 26.745	-16 07 21.82	$2.10 \pm 0.22$	$1.66 \pm 0.15$	$+0.4 \pm 0.3$	0".4
12	18 20 27.377	-16 11 38.59	$0.53 \pm 0.08$	$0.60 \pm 0.10$	$-0.2 \pm 0.4$	U
13	18 20 27.855	-16 09 55.60	$0.15 \pm 0.03$	$0.24 \pm 0.07$	$-0.9 \pm 0.7$	U
14	18 20 28.022	-16 11 27.00	$0.36 \pm 0.07$	$0.30 \pm 0.06$	$+0.3 \pm 0.5$	U
15	18 20 28.233	-16 13 17.83	$0.64 \pm 0.06$	$0.72 \pm 0.09$	$-0.2 \pm 0.3$	U
16	18 20 28.283	-16 11 30.53	$0.22 \pm 0.05$	$0.24 \pm 0.07$	$-0.2 \pm 0.7$	U
17	18 20 28.384	-16 10 14.13	$0.33 \pm 0.07$	$0.30 \pm 0.09$	$+0.2 \pm 0.7$	U
18	18 20 29.118	-16 08 58.61	$2.59 \pm 0.29$	$2.26 \pm 0.19$	$+0.3 \pm 0.3$	0".6
19	18 20 29.436	-16 10 49.84	$0.51 \pm 0.08$	$0.43 \pm 0.10$	$+0.3 \pm 0.5$	U
20	18 20 29.811	-16 10 45.58	$0.92 \pm 0.07$	$1.36 \pm 0.09$	$-0.7 \pm 0.2$	U
21 <sup>c</sup>	18 20 29.897	-16 10 44.45	$1.48 \pm 0.07$	$0.96 \pm 0.08$	$+0.8 \pm 0.2$	U
22	18 20 30.003	-16 10 35.26	$0.81 \pm 0.07$	$0.77 \pm 0.09$	$+0.1 \pm 0.3$	U
23	18 20 30.131	-16 10 39.45	$0.46 \pm 0.07$	$0.63 \pm 0.11$	$-0.6 \pm 0.4$	U
24	18 20 30.323	-16 10 50.65	$0.24 \pm 0.06$	$0.35 \pm 0.09$	$-0.7 \pm 0.7$	U
25	18 20 30.342	-16 11 43.67	$0.26 \pm 0.06$	$\leq 0.16 \pm 0.04$	$\geq +0.9 \pm 0.6$	U
26	18 20 30.415	-16 11 03.63	$0.27 \pm 0.07$	$0.18 \pm 0.06$	$+0.8 \pm 0.8$	U
27	18 20 30.442	-16 10 53.08	$0.24 \pm 0.06$	$0.48 \pm 0.09$	$-1.3 \pm 0.6$	U
28	18 20 30.577	-16 11 04.13	$0.80 \pm 0.07$	$0.69 \pm 0.08$	$+0.3 \pm 0.3$	U
29	18 20 30.632	-16 10 28.51	$0.31 \pm 0.06$	$0.17 \pm 0.05$	$+1.1 \pm 0.7$	U
30	18 20 30.777	-16 10 59.35	$0.98 \pm 0.08$	$0.74 \pm 0.08$	$+0.5 \pm 0.3$	U

Table 3—Continued

JVLA Number	Position <sup>a</sup>		Flux Density(mJy)		Spectral Index	Angular Size <sup>b</sup>
	$\alpha(2000)$	$\delta(2000)$	8.46 GHz	4.96 GHz		
31 <sup>c</sup>	18 20 31.112	-16 09 29.83	2.02±0.07	1.13±0.09	+1.1±0.2	U
32	18 20 31.523	-16 10 32.56	0.20±0.05	0.14±0.05	+0.7±0.8	U
33	18 20 32.981	-16 11 15.55	0.19±0.04	0.13±0.05	+0.7±0.8	U
34	18 20 33.060	-16 11 21.59	1.08±0.07	1.43±0.09	-0.5±0.2	U
35	18 20 33.090	-16 09 40.85	0.95±0.19	≤0.20±0.05	≥2.9±0.6	0''5
36	18 20 33.504	-16 10 44.57	0.49±0.08	0.40±0.08	+0.4±0.5	U
37	18 20 33.609	-16 10 21.66	0.22±0.05	0.29±0.06	-0.5±0.6	U
38	18 20 33.767	-16 10 46.39	0.26±0.06	0.27±0.08	-0.1±0.7	U

<sup>a</sup>From the 8.46 GHz data, except for source 1, where the position is from the 4.96 GHz data. The positional error is estimated to be  $\sim 0''.1$ . <sup>b</sup>U = Unresolved. <sup>c</sup>Time variable sources. The flux densities listed are the average of the three observing sessions.

Table 4: Counterparts to compact radio continuum sources in M17.

JVLA		Position <sup>a</sup>	
Number	Counterpart <sup>b</sup>	$\alpha(2000)$	$\delta(2000)$
3	2MASS J18201947-1613298	18 20 19.472	-16 13 29.89
4	CI* NGC 6618 B 335	18 20 21.435	-16 12 06.85
5	CI* NGC 6618 B 331	18 20 21.640	-16 11 18.00
8	CI* NGC 6618 B 267	18 20 25.500	-16 10 53.77
13	CI* NGC 6618 B 228	18 20 27.852	-16 09 56.04
15	[BFT2007] 471	18 20 28.260	-16 13 17.91
16	CI* NGC 6618 B 222	18 20 28.300	-16 11 31.19
19	CXOU J182029.4-161050	18 20 29.439	-16 10 50.22
20	CEN 1b = [PCB2009] 2	18 20 29.811	-16 10 45.67
21	CEN 1a = [PCB2009] 1	18 20 29.900	-16 10 44.40
22	CXOU J182030.0-161034	18 20 30.030	-16 10 34.81
23	CXOU J182030.0-161039	18 20 30.080	-16 10 39.97
25	CI* NGC 6618 B 179	18 20 30.346	-16 11 43.69
27	CI* NGC 6618 B 174	18 20 30.448	-16 10 53.09
28	2MASS J18203057-1611040	18 20 30.578	-16 11 04.10
29	SSTGLMC G015.0618-00.6890	18 20 30.649	-16 10 28.25
31	CI* NGC 6618 B 159	18 20 31.115	-16 09 29.88
32	2MASS J18203152-1610326	18 20 31.523	-16 10 32.61
34	CI* NGC 6618 B 137	18 20 33.061	-16 11 21.56

<sup>a</sup>Position from the SIMBAD Astronomical Database. <sup>b</sup>2MASS = 2 Micron All-Sky Survey; CI\* NGC 6618 = Star in cluster NGC 6618; B = Bumgardner (1992); BFT = Broos et al. (2007); CXOU = Chandra X-ray Observatory, Unregistered; PCB = Povich et al. (2009); SSTGLMC = Spitzer Space Telescope Galactic Legacy infrared Mid-Plane survey.

Table 5: Flux densities for CEN 1a and CEN 1b.

Source	Frequency (GHz)	2011 Jun 16 (mJy)	2011 Jun 27 (mJy)	2011 Jul 28 (mJy)
CEN 1a	4.96	$\leq 0.27 \pm 0.09$	$\leq 0.21 \pm 0.07$	$2.69 \pm 0.09$
CEN 1a	8.46	$\leq 0.26 \pm 0.05$	$\leq 0.24 \pm 0.06$	$2.58 \pm 0.05$
CEN 1a	22.46	—	$\leq 0.42 \pm 0.10$	—
CEN 1b	4.96	$1.17 \pm 0.10$	$1.17 \pm 0.11$	$1.15 \pm 0.09$
CEN 1b	8.46	$0.81 \pm 0.05$	$0.66 \pm 0.06$	$0.80 \pm 0.05$
CEN 1b	22.46	—	$\leq 0.42 \pm 0.10$	—

Table 6: Flux densities for NGC 6618 B 159.

Frequency (GHz)	2011 Jun 16 (mJy)	2011 Jun 27 (mJy)	2011 Jul 28 (mJy)
4.96	1.89±0.09	1.67±0.13	≤0.21±0.06
8.46	3.82±0.07	1.61±0.06	≤0.18±0.04
22.46	—	≤1.56±0.42	—